Management Systems in Production Engineering

2026, Volume 34, Issue 4, pp. 631-647

Date of submission of the article to the Editor: 05/2026
Date of acceptance of the article by the Editor: 10/2026

DOI 10.2478/mspe-2026-0053

FINITE ELEMENT SIMULATION OF THE POLISHING PROCESS FOR ALUMINUM WORKPIECES IN THE LS-DYNA SOFTWARE



Sergei Bratan
Sevastopol State University

Milan Sága
University of Žilina

Andrei Pakhaliuk, Vladimir Pakhaliu
Sevastopol State University

Jiří Kuchař
Czech Technical University in Prague

Boris Yakhimovich
Sevastopol State University

Abstract:
Finishing of long cylindrical aluminium components increasingly relies on abrasive belt machining, yet dependable guidelines for selecting its operating regimes remain scarce. To help close this gap, the present work applies explicit dynamic finite element modelling in LS-DYNA to reproduce, at the scale of a single abrasive grain, how the surface of a 6061-T6 alloy is generated during belt polishing. Two idealised grain geometries are contrasted: a truncated cone standing for a fresh abrasive and a half-ellipsoid approximating the same grain after wear. The material response is captured through the Johnson-Cook constitutive and fracture relations together with a Mie-Grüneisen equation of state, so that high strain rates, frictional heating and element erosion are reflected. For each geometry the resultant contact force, the total, sliding and workpiece-side energies, the actual contact area, the contact-zone temperature, the chip morphology and the residual groove profile were examined while the sliding velocity, the indentation depth and the friction coefficient were varied. The computations show that wear-driven rounding of the grain reduces the polishing force at low speeds but simultaneously raises the dissipated energy and the local heating, whereas the conical grain leaves a smoother groove under milder thermal loading. Near a practical belt speed of about 5 m/s the predicted temperature rise stays limited, and grain shape combined with cutting depth governs the attainable finish more strongly than speed alone. These findings offer a physically grounded basis for choosing rational polishing conditions and for deciding when a worn belt should be replaced.

Key words: LS-DYNA, polishing simulation, Johnson-Cook model, Grüneisen equation of state, ellipsoidal and truncated conical grain

INTRODUCTION

The transition to a market economy has highlighted the challenges associated with producing competitive products in mechanical engineering and instrument making. "Consumers demand products whose characteristics meet their needs and expectations" [1, 2, 3]. An analysis of modern research in the field of finishing suggests an increasing demand for the production of polished long aluminum tubes and

© 2026 Author(s). This is an open access article licensed under the Creative Commons BY 4.0 (https://creativecommons.org/licenses/by/4.0/)

other cylindrical workpieces. The most effective method for finishing such products is belt polishing [4]. The widespread adoption of this method in production is hampered by the lack of clear processing techniques for these materials. Polishing is a rather complex process. To determine its rational parameters, which contribute to improved processing quality and increased productivity, it is necessary to integrate numerical modeling technology into this field. This is achieved through finite element modeling to perform a dynamic analysis of the process itself, as well as to study the interactions and patterns of change in its parameters. This approach allows for a significant reduction in the cost and time required for its implementation compared to experimental studies.

In recent decades, research has been conducted to improve polishing results, including increasing the material removal rate, increasing the cutting speed, and other parameters. All of these advances are based on a thorough study of the cutting mechanism during single-grain polishing. Parameters such as grain shape and material, grain speed (belt speed), processing depth, and the quality of the surface obtained on the workpiece are important in studying the polishing process. A study with a single grain makes it possible to identify the influence of these parameters with lower machine time costs, since calculations can last from 0.5 to 15 hours or more, depending on the grain speed (the lower the speed, the longer the calculation). With a more complex model, the calculation time can increase even more. LS-DYNA software is used in international practice to carry out such research. In the literature [5], for example, using LS-DYNA, a finite element study of the grinding process for a steel workpiece using a single grain in the shape of only a truncated cone was performed, while the grain can have other shapes. However, in the cited work, the authors' primary objective was to demonstrate the feasibility of using a convenient formulation of the finite element method – the smooth particle hydrodynamics (SPH) method. In [6], a finite element study of the cutting properties of a single grain in the shape of a traditional truncated cone and a cone with a spherical cutting edge was conducted on a steel workpiece. However, the ductility and fracture properties of aluminum alloys differ significantly from those of steel, and therefore, the conclusions reached in the study cannot be directly applied to polishing of alloys and require appropriate verification and adjustment. In [7], the properties of aluminum alloy A357 were studied at various cutting speeds using finite element analysis, but with a cutter of varying shapes to determine the moment of chip formation.

Industrial and reliability-oriented studies emphasize that surface preparation and polishing quality significantly influence long-term functional performance. The influence of surface pretreatments on the reliability of bonded joints was analyzed in [8], where controlled surface conditioning were shown to improve adhesion strength and reduce defect initiation sites. Maintenance and cleaning strategies for heat exchangers [9] demonstrated that surface finish quality directly affects fouling behavior, corrosion resistance, and thermal efficiency. Similarly, mitigation of risks in energetic facilities through systematic cleaning of internal surfaces [10] highlighted the importance of minimizing surface irregularities and contamination to prevent degradation processes. The mitigation of corrosion and delamination risks through optimized surface pre-treatment procedures [11] confirmed that appropriate polishing and cleaning strategies reduce stress concentrators and improve long-term structural stability.

From the perspective of polishing mechanisms and hybrid processes, chemical mechanical polishing (CMP) of aluminum alloys using alumina-based slurry was investigated in [12], demonstrating that abrasive particle size and slurry pH significantly affect the balance between mechanical micro-cutting and chemical surface activation, thereby influencing material removal rate and final surface roughness. Advanced tool concepts were presented in [13], where polishing of aluminum alloy optical elements with a new solid flexible bonnet tool improved pressure distribution control and surface form accuracy. In [14], acoustic energy-assisted polishing of 2024 aluminum alloy combined experimental and numerical approaches, revealing intensified stress localization and enhanced chip formation efficiency under acoustic excitation.

For internal cylindrical geometries, spiral-rotating abrasive flow polishing was analyzed numerically and experimentally in [15], where CFD simulations confirmed the influence of abrasive flow velocity,

turbulence intensity, and pressure distribution on surface finish evolution in 6061 aluminum alloy. Thermal hazards associated with aluminum tube polishing were documented in [16], identifying excessive frictional heating and accumulation of fine aluminum particles as potential ignition sources under high cutting speeds and insufficient cooling.

Alternative finishing technologies further extend the understanding of surface formation mechanisms. Electropolishing of single-crystal and polycrystalline aluminum was theoretically analyzed in [17], showing that crystallographic orientation influences dissolution kinetics and achievable optical smoothness. A mechanistic study of surface plastic flow during polishing [18] demonstrated that material redistribution and micro-scale plastic deformation significantly contribute to surface smoothing alongside abrasive micro-cutting.

High-precision machining studies also confirm the relationship between cutting parameters and final surface quality. In [19], high-precision turning combined with ultra-smooth direct polishing of aluminum alloy mirrors achieved nanometric roughness levels, emphasizing the role of optimized cutting speed and tool condition. Laser polishing of ground aluminum surfaces [20] revealed that scanning speed and energy density determine remelting depth and surface smoothing efficiency. Furthermore, [21] demonstrated that coating and polishing of cutting tools improve the machined surface integrity in dry machining of aluminum alloys, positively affecting subsequent polishing performance.

Numerical and analytical modeling approaches provide further insight into surface generation mechanisms [22]. Modeling and simulation of surface generation in lapping and polishing [23] clarified abrasive-workpiece interaction mechanisms, including micro-cutting and impact phenomena [24, 25]. Analytical estimation of polishing time for different metallic alloys [26] incorporated relative velocity and material constants into predictive formulations of surface evolution. Theoretical and experimental investigation of surface texture evolution during polishing [27] emphasized the interaction between abrasive kinematics and material flow behavior in determining final topography [34]. Alloy fatigue is also taken into account as stated by [35].

The objective of this work is to evaluate the performance of belt polishing for aluminum alloy workpieces using truncated cone and ellipsoid-shaped grains using the LS-DYNA software.

MATERIALS AND METHODS

Geometric Model

It is known that with fine polishing, the surface roughness R_a is 0.1-0.4 μm, while with mirror polishing, it is < 0.05 μm. Moreover, the grain size on the abrasive belt according to the European classification (FEPA P) for P500-P1200 is 20-10 μm, and for P800-P2500, 14-3 μm. Due to the small grain size and the resulting small dimensions of the "grain-workpiece" model itself, the LS-DYNA solver encounters very small masses, below the processor's single-precision capabilities. For this reason, a grain height of 20 μm was chosen, eliminating this problem with single-precision calculations. Using double-precision calculations would have significantly increased the computational resource.

Fig. 1a shows a 3D "grain-workpiece" model, where the grain has the shape of a truncated cone with the height dimensions H_c = 0.02 mm, the major radius R_c = 0.01 mm and the minor radius r_c = 0.0025 mm. This grain shape can exist at the beginning of polishing with a new belt. The workpiece is represented in the shape of a rectangular parallelepiped with the length dimensions L = 0.03 mm, the width B = 0.02 mm and the height H = 0.015 mm. The grain and the workpiece do not necessarily have to be in initial contact. Fig. 1b shows a similar 3D model, but the grain has the shape of half an ellipsoid with the height dimension a = 0.01 mm (the major semi-axis), the radius of curvature r = 0.01 mm and the minor semi-axis b = 0.00625 mm. This is approximately the grain shape that occurs after the wear of the truncated cone during operation.

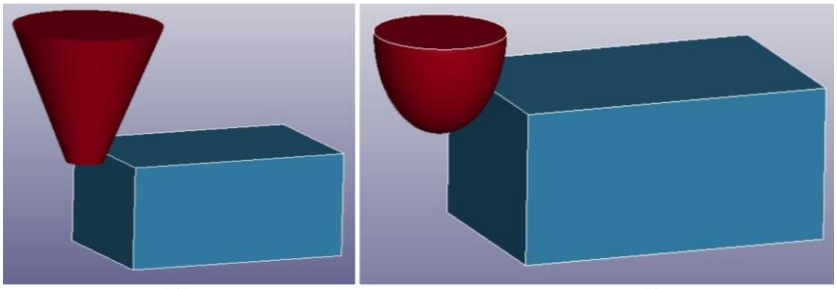


Fig. 1 3D model of "grain-workpiece", where the grain has the shape of: a) a truncated cone; b) half an ellipsoid
Alt-text: *3D CAD view of a dark-red abrasive grain above a blue workpiece block: a) grain as an inverted truncated cone; b) grain as a half-ellipsoid.*

Boundary conditions

The grain's movement is constrained by one degree of freedom for translational motion at a constant speed along the workpiece, namely the polishing speed, along the Y-axis for the cone model and along the X-axis for the ellipse model. The workpiece is fixed along its lower surface by constraining all degrees of freedom.

Material modeling

The following units were adopted for the LS-DYNA simulation: mm, grams, milliseconds (ms), °C, and MPa. The polishing grain was also assumed to be made of a common abrasive material, alumina ceramics (Al2O3), which was modeled as a perfectly rigid body (*MAT_RIGID) with the following mechanical properties [28]: density ρ = 0.00389 g/mm^3, elastic modulus E = 375 GPa, and Poisson's ratio ν = 0.22. The grain was defined as a perfectly rigid body, as this is a standard approach for saving computational resources, as its finite elements are not involved in solving the integral equations of contact with the workpiece.

The widely used 6061-T6 aluminum alloy was used as the workpiece material, as it has experimentally confirmed parameters required for the calculations. This material is adopted as an object in this problem, since the aim of the work is a relative study of the polishing process using grains with two different shapes. The thermomechanical characteristics of the workpiece material are as follows [28]: density ρ = 0.0027 g/mm^3; elastic modulus E = 68.9 GPa; Poisson's ratio ν = 0.33; melting point T_m = 650°C; specific heat capacity C_m = 896 mJ/(g°C). The Johnson-Cook model was used as a model of the workpiece material. This model of plasticity is widely used in simulating high-speed metalworking, since it allows for high deformation rates and temperature effects, which are the determining characteristics of chip formation during polishing. The model includes temperature dependence through thermal softening parameters. When polishing aluminum, local heating occurs in the contact zone of the abrasive with the surface, which significantly affects the mechanical properties of the material. This model is implemented in LS-DYNA as *MAT_JOHNSON_COOK (JC) and has the following general form [7]:

$$\sigma = \left[A + B\varepsilon_p^n\right]\left[1 + C\ln\frac{\dot{\varepsilon_p}}{\dot{\varepsilon}_0}\right]\left[1 - \left(\frac{T - T_r}{T_m - T_r}\right)^m\right], \quad (1)$$

where:
σ is the effective stress,
ε_p the effective plastic strain,
$\dot{\varepsilon}_p$ and $\dot{\varepsilon}_0$ are the effective and reference strain rates,
T, T_r and T_m are the current, room and melting temperatures.
For the specified alloy, the parameter values are defined in [29]: A is the initial yield strength; B is the hardening coefficient; n is the hardening exponent; C is the strain rate sensitivity coefficient; m is the thermal softening exponent. Chip formation was modeled using the Johnson-Cook fracture law. In this law, strains, strain rates and temperatures are taken into account as in Eq. (2):

$$\varepsilon_f = [D_1 + D_2 \exp(D_3\sigma^*)]\left[1 + D_4 \ln\frac{\dot{\varepsilon_p}}{\dot{\varepsilon_0}}\right]\left[1 + D_5\left(\frac{T - T_r}{T_m - T_r}\right)^m\right], \quad (2)$$

where:
σ* is the ratio of hydrostatic pressure to equivalent stress, and the coefficients define:
D_1 is the initial strain before failure;
D_2 is the effect of stress triaxiality;
D_3 is the sensitivity to stress triaxiality;
D_4 is the sensitivity to strain rate;
D_5 is the sensitivity to temperature at failure.
Failure is then allowed to occur when the damage parameter D, defined by Eq. (3), reaches unity (D = 1.0), and therefore all relevant particles are excluded from the calculations:

$$D = \sum\frac{\Delta\varepsilon_p}{\varepsilon_f}. \quad (3)$$

In LS-DYNA, the *MAT_JOHNSON_COOK model describes only the deviatoric (shear) part of stresses and temperature-dependent plasticity, but does not define the equation of state (EOS) for hydrostatic pressure. Therefore, to correctly calculate the full stress tensor for impact/high-speed processes, separate parameters are required, most often EOS_GRUNEISEN, which determine the relationship between pressure, volumetric strain, and internal energy of the material. The Mie-Grüneisen equation of state defines pressure as the sum of the shock adiabat and a thermal energy additive, relating pressure to density and internal energy, which is critical for shock waves, chip detonation, and strong volumetric compression/heating. In explicit impact/cutting problems, the full stress tensor is composed as the sum of the hydrostatic (from EOS) and deviatoric (from JC) parts. Without EOS, the pressure will be uncertain or incorrect, leading to errors in the wave response, temperature coupling, and triaxially sensitive failure criteria. To accurately calculate the hydrostatic component of deviatoric stresses for compression, the Grüneisen Eq. (4) is used [30]:

$$\rho = \frac{\rho_0 C^2 \mu\left[1 + \left(1 - \frac{\gamma_0}{2}\right)\mu - \frac{a}{2}\mu^2\right]}{\left[1 - (S_1 - 1)\mu - S_2\left(\frac{\mu^2}{1+\mu}\right) - S_2\left(\frac{\mu^2}{(1+\mu)^2}\right)\right]^2} + (\gamma_0 + a\mu)E_0 \quad (4)$$

and for stretching Eq. (5):

$$\rho = \rho_0 C^2 \mu + (\gamma_0 + a\mu)E_0 \quad (5)$$

the compression ratio is equal to Eq. (6):

$$\mu = \frac{\rho}{\rho_0} - 1, \quad (6)$$

where is the pressure:
ρ_0 is the reference density, is the speed of sound in the material,
γ_0 is the Grüneisen gamma,
S_i are the slope constants characteristic of a particular material,
α is the volume correction factor,
E_0 is the tensile modulus of elasticity.
The strength and damage constants of the Johnson-Cook model, considered in the obtained modeling results and included in Eqs. (1)-(3), are presented in Table 1 [29]. The coefficients included in the Grüneisen equations Eqs. (4)-(6) are listed in Table 2 [30, 31, 32, 33].

Table 1
Johnson-Cook constants for aluminum alloy 6061-T6

A, MPa	B, MPa	n	C	m	D_1	D_2	D_3	D_4	D_5
324	114	0.42	0.002	1.3	-0.77	1.45	-0.47	0.0	1.6

Source: [29].

Table 2

Grüneisen equation coefficients for aluminum alloy 6061-T6

C, m/s	1	2	γ_0	α
5330	1.338	0	1.97	0.48

Source: [30, 31, 32, 33].

Contact interaction

The contact interaction between the grain and the workpiece was modeled using the CONTACT_ERODING_SURFACE_TO_SURFACE contact – a standard surface-to-surface penalty contact with additional logic for updating the contact surface when solid elements are eroded according to the failure criterion. Thus, in the eroding contact, LS-DYNA rebuilds the list of outer segments after each step, taking into account the removed elements, and all destroyed elements are removed.

Finite element partitioning

To ensure solution accuracy, the mesh element sizes were chosen such that the grain had at least seven elements in the grain-workpiece contact plane, and the workpiece had ten elements. Hexagonal "bricks" elements of Solid 164 from LS-DYNA were adopted for both the grain and the workpiece, as they provide the most accurate solution. For the grain, the element sizes were assigned, and the mesh was generated using the sweep method for its conical shape, and the mapped method for its semi-ellipsoidal shape. The correctness and uniformity of the mesh are confirmed by solving a problem where the hourglass energy parameter is very small compared to other energy parameters. In this case, it was found to be three orders of magnitude smaller, confirming the validity of this solution.

RESULTS AND DISCUSSION

Studied Parameters

The results of solving the problem in LS-DYNA are written to a d3post file, which can be opened in LSPrepost, from which the desired parameters can be obtained. Parameters were selected for the study that reflect the force interaction in the contact and the energy interaction, which, in turn, also allows for the evaluation of the temperature component in the contact. These parameters are as follows:

a) Resultant force is the total contact force acting between the grain and the workpiece (the summed vector result of the normal and tangential components for all active contact points in a given contact). It represents the instantaneous "contact force" between the grain and the workpiece, integrated over the entire contact zone, i.e., it is the modulus of the polishing force in the form $\sqrt{F_x^2 + F_y^2 + F_z^2}$
b) Total energy is the energy accumulated/"experienced" in a given contact, i.e., the total work of the contact forces (normal + tangential) during the calculation. Includes contributions from both the normal component (indentation/elastoplastic deformation) and friction (sliding).
c) Sliding energy is the energy associated solely with the tangential component of the contact force, i.e., the work done by frictional forces during relative sliding of surfaces. For polishing applications, it most closely correlates with heat generation in the surface layer, the intensity of grain wear, and the quality of the machined surface.
d) Slave energy is this value refers to the “slave” (workpiece) side of the contact and shows what part of the contact work/energy is attributed to this side.

To evaluate these parameters, calculations were performed and diagrams were obtained for their change depending on the grain sliding velocity and its penetration depth for truncated cone and semi-ellipsoid grains. A friction coefficient of 0.3 was adopted in the calculations, as for dry polishing. As an example, the curve of the resulting polishing force for a conical grain at a moving speed of 5 m/s and a penetration depth of 0.001 mm, interacting between the grain and the workpiece, is shown in Fig. 2. It is evident that deepenings are observed in the contact force graph during polishing.

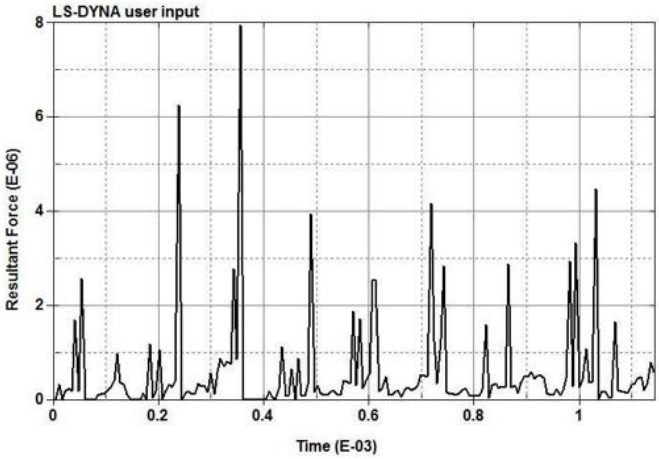


Fig. 2 Graph of the resulting force (N) for a conical resulting force for grain at a speed of 5 m/s and a depth of 0.001 mm

Alt-text: *Line graph of resultant force versus time; an irregular low signal near zero with sharp intermittent peaks reaching about 8 (×10⁻⁶ N).*

This is because each finite element of the workpiece undergoes plastic deformation during polishing, thereby breaking and removing it. A gap then forms between the grain and the workpiece in contact, where the force can acquire a zero value, i.e., a break in polishing occurs. In addition, the grain and the workpiece do not contact the same point of force application, so the polishing result also varies. Diagrams of the change in the average value for the resulting force as a function of grain velocity and penetration depth for truncated cone- and semiellipsoid-shaped grains, is shown in Fig. 3. Figs 4, 5, and 6 similarly present diagrams of the total energy, sliding energy, and slave energy. Another important indicator is the ratio of sliding energy to total energy, which can be used to estimate the proportion of heat from friction, i.e., its contribution to the total energy.

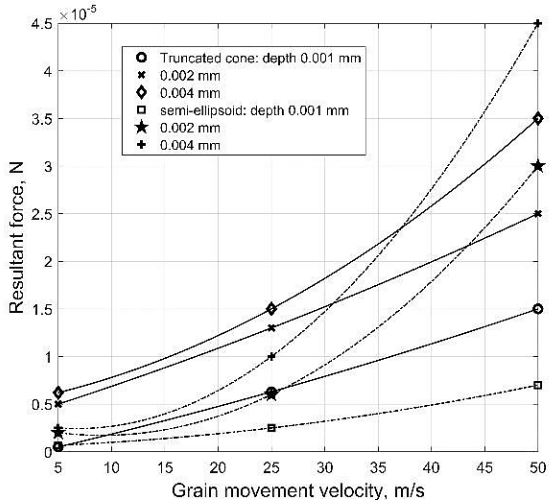


Fig. 3 Graphs of the average resulting force for grain at two grain shapes at different depths and speeds of its movement

Alt-text: *Line graph of resultant force versus grain velocity (5-50 m/s) for cone and semi-ellipsoid grains at depths 0.001, 0.002 and 0.004 mm.*

Long description: *six upward curves. The cone curves are highest at low speed and rise steadily; the ellipsoid curves start lower but climb more steeply and overtake the cone curves at high velocity, most clearly at 0.004 mm depth.*

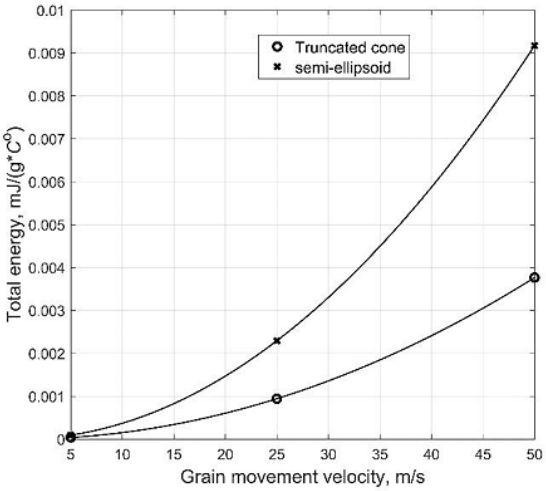


Fig. 4 Graphs of total energy for two forms of grain with a change in the speed of its movement
Alt-text: *Line graph of total energy versus grain velocity (5-50 m/s); two upward-curving lines, the semi-ellipsoid consistently above the truncated cone.*

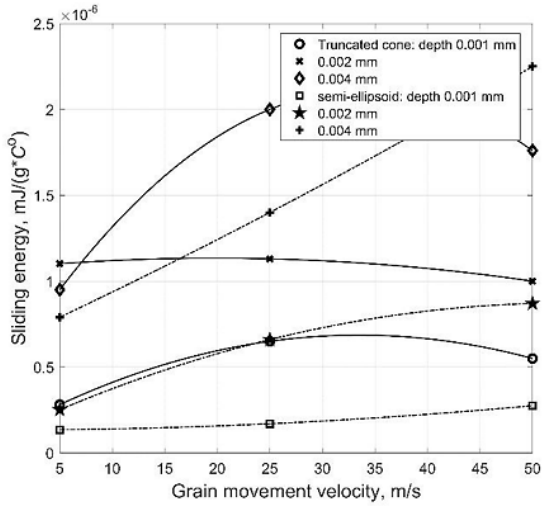


Fig. 5 Graphs of sliding energy for two forms of grain at different depths and speeds of its movement
Alt-text: *Line graph of sliding energy versus grain velocity (5-50 m/s) for truncated-cone and semi-ellipsoid grains at depths 0.001, 0.002 and 0.004 mm.*

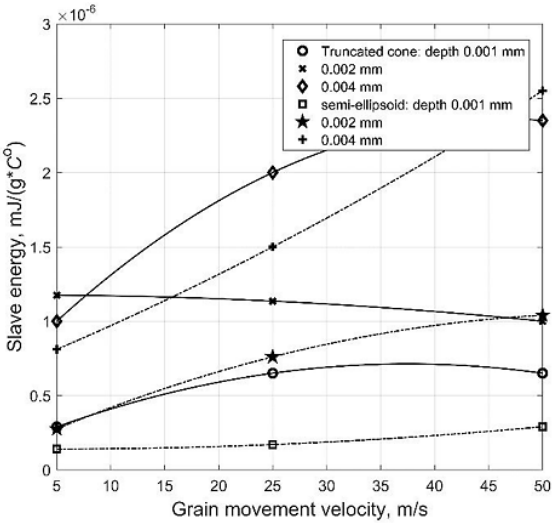


Fig. 6 Slave energy graphs for two grain shapes sliding energy with changes in depth and speed of movement
Alt-text: *Line graph of slave-side contact energy versus grain velocity (5-50 m/s) for cone and semi-ellipsoid grains at depths 0.001, 0.002 and 0.004 mm.*

Fig. 7 shows this for the two grain shapes, as a function of grain velocity and penetration depth.

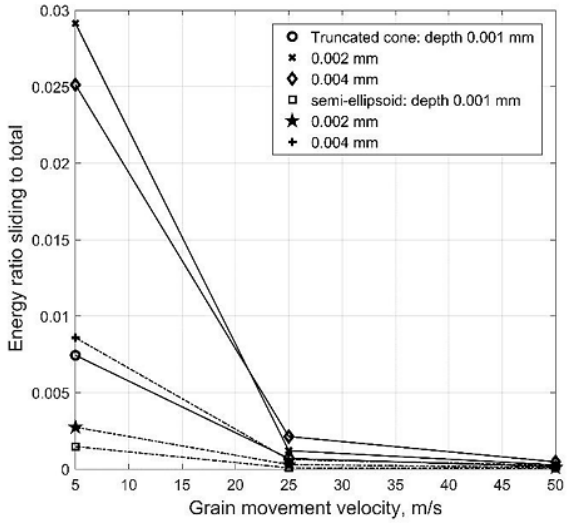


Fig. 7 Graphs of the relationship for sliding energy to total energy for two grain shapes at different grain velocity

Alt-text: *Line graph of the sliding-to-total energy ratio versus grain velocity; all curves fall steeply from 5 to 25 m/s and approach zero by 50 m/s.*

An analysis of Fig. 3 shows that with increasing grain velocity, the intensity of the increase in the resulting force for an ellipsoid at a penetration depth of 0.002 mm and above is greater, especially when approaching 50 m/s, than for a truncated cone. However, at a speed of approximately 5 m/s, which is most suitable for polishing aluminum workpieces, the forces for both grain shapes are approximately equal at a depth of 0.001 mm and are approximately twice as large for a truncated cone, starting at a depth of 0.002 mm. The change in total energy with grain penetration depth is negligible and depends only on the grain velocity, being significantly greater for an ellipsoid, as can be seen in Fig. 4.

From the above, it follows that as the grain, initially shaped like a truncated cone, wears toward an ellipsoid, the resulting contact force for low speeds (polishing) decreases, but the energy component, in the form of the total energy expended, increases. Fig. 5 shows the dependences of the sliding energy on the grain velocity for a truncated cone and an ellipsoid at different penetration depths. It is evident that for a truncated cone-shaped grain, the energy is higher and changes insignificantly with increasing velocity, tending to decrease slightly with increasing velocity. However, at a depth of 0.004 mm for an ellipsoid, it continuously increases. The decrease in energy can probably be explained by the fact that, with increasing velocity, the workpiece material beneath the grain transforms into a softer layer of plastic flow, along which the grain can "float" with less expended energy. The dependences for the slave energy, shown in Fig. 6, practically repeat the shapes of the diagrams in Fig. 5, which demonstrates a correlation between them, since as the sliding energy decreases, the energy supplied to the workpiece also decreases. The ratio of sliding energy to total energy in Fig. 7 shows that sliding energy has the greatest contribution for conical grains and decreases significantly for both grain shapes as the grain velocity increases, where at 25 m/s it is already less than 5%, and even less for ellipsoidal grains.

At a polishing speed of 5 m/s, the contribution of ellipsoidal grain to the resulting force is no more than 10% for all penetrations, while for conical grain, it reaches almost 30% for a 0.002 mm penetration, decreasing to 25% for a 0.004 mm penetration.

The influence of the friction coefficient on the resulting force for two grain shapes, depending on the penetration depth, was also studied for a given grain speed. Fig. 8 shows a comparison of the average force values for friction coefficients of 0.1 and 0.3.

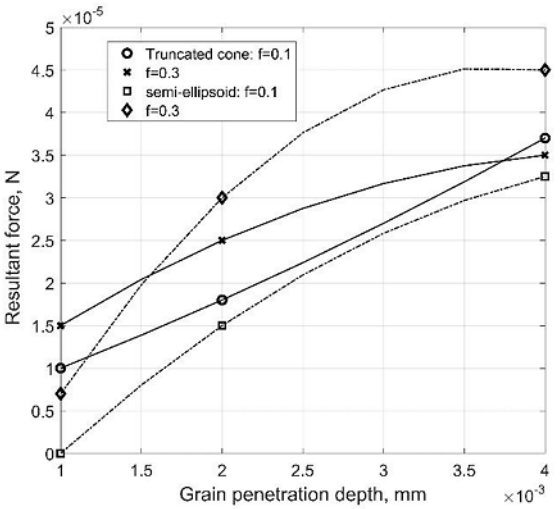


Fig. 8 Graphs of the average resultant force for two its grain shapes with changes in the friction coefficient and of grain penetration depth

Alt-text: *Line graph of resultant force versus grain penetration depth (0.001-0.004 mm) for cone and semi-ellipsoid grains at friction coefficients 0.1 and 0.3.*

It is evident that the influence of the ellipsoid shape is greater than that of the conical shape.

Determination of temperature in the contact zone

Almost all-frictional work is converted into heat in the contact zone (usually the conversion coefficient is η ≈ 0.9-1.0). The sliding energy E_{slid} must be used as the source of frictional heat generation. Then, the amount of heat generated in the contact zone can be estimated taking into account the coefficient α of the proportion of heat lost to the workpiece (α = 0.8-0.95 for polishing aluminum with an abrasive tool), as:

$$Q\text{slid} \approx \eta\alpha E\text{slid}. \tag{7}$$

The average specific heat flow in the polishing zone in this case can be represented by the dependence

$$q \approx \frac{\Delta Q_{slid}}{A_{act}\Delta t}, \tag{8}$$

where:

A_{act} is the actual contact area;

Δt is the time interval $[t_1,t_2]$ over which the increment in sliding energy ΔE_{slid} is taken and the amount of heat ΔQ_{slid} released is estimated using Eq. (7).

The actual contact area A_{act} for a grain at a given cutting depth depends on the grain geometry and the depth of its penetration into the workpiece. For a truncated cone, the contact area at the cutting depth is the area of the annular pad on the lateral surface generated by the intersection of the cone and the workpiece plane at the specified axial penetration depth. For a semiellipsoid, the contact area is the area of the elliptical "droplet" contact patch of the semiellipsoid when penetrating to the specified depth. During steady transverse penetration (without significant forward shear or slippage), only the tangential contact area (contact surface) is usually considered, that is, the geometric contact patch between the grain and the workpiece at a given instant. For small cutting depths, this is usually taken as the base area at level h. This approach is entirely acceptable, since only a relative comparison of the contact area of two grain shapes under identical determination conditions is of interest. Then, for a conical grain, the actual contact area is:

$$A_{act\,c} = \pi R_h^2, \tag{9}$$

where:

R_c, r_c, H_c are the major radius, minor radius and height of the truncated cone;

$R_h = r_c\,(R_c - r_c)\frac{h}{H_c}$ is the radius of the conical surface at the penetration depth h.

For small penetration depths, the contact area of an ellipsoid is an ellipse with a major semi-axis a_{el} and a minor semi-axis b_{el} , which depend on the geometry and depth:

$$a_{el} = a\sqrt{\frac{2h}{H_{el}}},\ b_{el} = \sqrt{\frac{2h}{H_{el}}}, \tag{10}$$

where:
a, *b* are the major and minor semi-axes of the ellipsoid;
H_{el} is the height of the semiellipsoid.
The actual contact area for a semi-ellipsoidal grain, taking into account Eq. (10), is determined as

$$A_{act\ el} = \pi a_{el} b_{el} \tag{11}$$

Fig. 9 shows diagrams of the change in the actual grain contact area depending on the penetration depth for a truncated cone according to Eq. (9) and for a semi-ellipsoid according to Eq. (11).

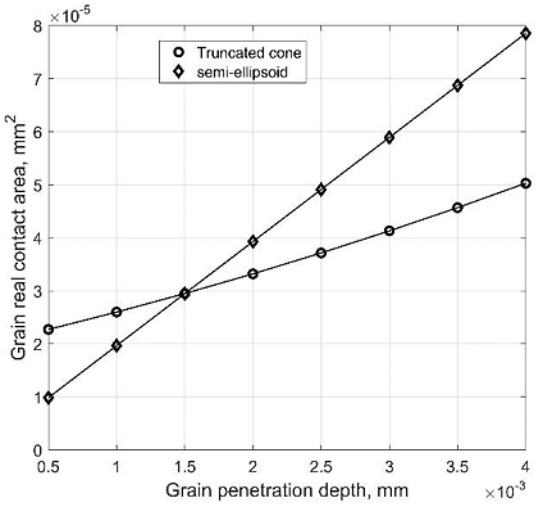


Fig. 9 Graphs of the actual grain area for two of shapes at different depths and the same speed movement
Alt-text: *Line graph of real grain contact area versus penetration depth (0.0005-0.004 mm); the cone and semi-ellipsoid lines cross near 0.0015 mm.*

It is evident that at a penetration depth of less than 0.0015 mm, the contact area for a semi-ellipsoid is smaller than for a truncated cone.
Now, based on the average heat flux across the contact pad, we can estimate the temperature increase on the workpiece surface using various approximate methods. We will use the method of estimating temperature based on the law of thermal conductivity. Assuming that heat is transferred only to the workpiece (a one-dimensional problem with ideal thermal contact), then:

$$q_m = -k\frac{\Delta T}{\Delta \delta}, \tag{12}$$

where:
q_m is the average heat flow;
k is the thermal conductivity coefficient of the workpiece;
δ is the heating thickness (characteristic layer, usually the cutting depth);
Δ*T* is the temperature difference between the surface and the “cold” inner layer.
Hence:

$$\Delta T = \frac{q\delta}{k} \tag{13}$$

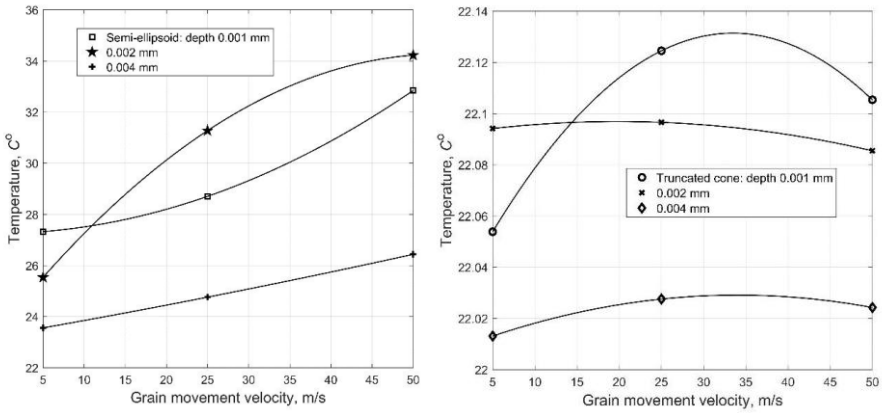
If heat is supplied to a small layer in a short time (for example, at a cutting depth h), then the instantaneous temperature increment (for a heat pulse):

$$\Delta T = \frac{q_m \Delta t}{\rho c_p h}, \tag{14}$$

where:
ρ is the material density;
c_p is the specific heat capacity;
Δt is the heat supply time.
If the contact area is a small spot and cooling occurs in the body mass (point source approximation), then the steady-state temperature is determined as:

$$T_{max} = T_0 + \frac{q_m a}{k}\sqrt{\frac{\pi}{\alpha}}, \tag{15}$$

where:
T_0 is the initial temperature; a is the characteristic size of the spot (radius of the contact spot);
$\alpha = \frac{k}{\rho c_p}$ is the thermal diffusivity.
Expression Eq. (15) gives an estimate of the maximum overheating on the surface under the spot during "instantaneous" established contact. For the adopted aluminum alloy of the workpiece material, using expressions Eqs. (14) and (15), the following parameters were applied, taking into account the workpiece length L = 0.03 mm: Δt = 0.006; 0.0012; 0.0006 ms is the time it takes for the grain to travel the length of the workpiece at a speed of v = 5; 25; 50 m/s; ρ = 0.0027 g/mm^3 is the density of the workpiece material; c_p = 896 mJ/(g °C); T_0 =22°C. Fig. 10a shows the diagrams of the temperature change depending on the grain movement speed and the depth of its penetration for a semi-ellipsoid, and Fig. 10b the same for a truncated cone.



a) *b)*

Fig. 10 Temperature graphs with changes in the speed of movement and depth of penetration for grain: a) ellipsoidal; b) conical

Alt-text: *Two temperature-versus-velocity graphs on different scales: a) semi-ellipsoid grain, about 24-34°C; b) truncated-cone grain, near 22.0-22.13°C.*

Long description: *In panel a the temperature rises with velocity and penetration depth up to roughly 34°C. In panel b the values stay close to room temperature (about 22.02-22.13°C), changing only slightly and peaking around 30-35 m/s.*

The diagrams are constructed on different figures due to the difference in scale in order to visualize them well, since for a conical grain the temperature at the workpiece is practically equal to the initial one and changes negligibly little with depth and speed of movement.
An analysis of the diagrams in Fig. 10a shows that for an ellipsoidal grain, the temperature increases with increasing velocity, but its gradient decreases with increasing penetration depth, likely due to heat dissipation across a larger volume of surrounding material. Thus, the change in grain shape from a truncated cone to an ellipsoid during wear leads to an increase in workpiece temperature, but when polishing at low speeds (5 m/s), the increase is approximately 13% for a depth of 0.001 mm, at most. The rate of temperature increase is approximately 460°C/ms. For greater penetration depths at the same grain velocity, the intensity of the temperature increase will be less.

Chip formation

Fig. 11 shows the formation of a plowing furrow on a workpiece when it is passed by both grain shapes.

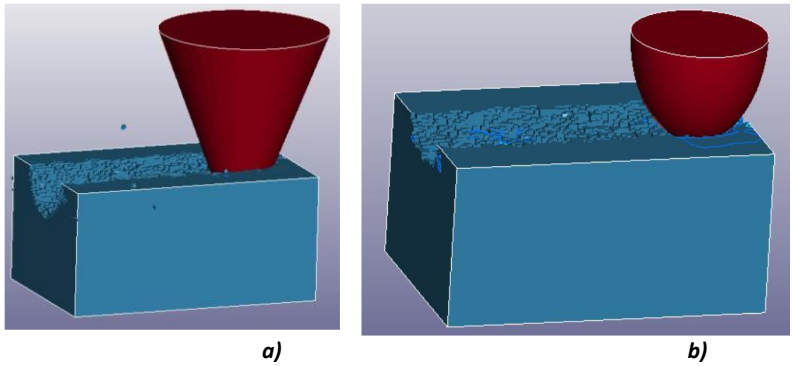


Fig. 11 Image of a plowing furrow on a workpiece from grain: a) conical; b) ellipsoidal

Alt-text: *Two 3D simulation views of a red abrasive grain ploughing a furrow along a blue workpiece: a) conical grain; b) ellipsoidal grain.*

It is evident that the chips are formed at the sides and are of small height, "ragged". In Fig. 12, it is shown in an enlarged form with an additional image of the von Mises equivalent stresses.

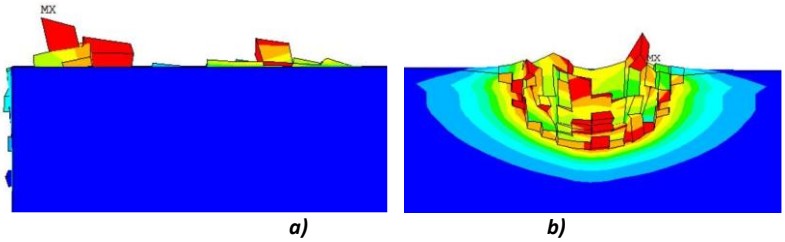


Fig. 12 Enlarged image of chips on a workpiece: a) from the side; b) in the transverse direction

Alt-text: *Two enlarged colour-contour cross-sections of chips at the workpiece surface: a) side view; b) transverse view, with chips concentrated at the top.*

This form of chip formation is understandable, since the conical and ellipsoid grain shapes have a negative rake angle, which does not allow the formation of a complete solid chip. When a furrow is formed, the remaining part of the workpiece material is removed into the surrounding space, which is clearly shown in Fig. 13, where the grain deepening is made to 0.006 mm.

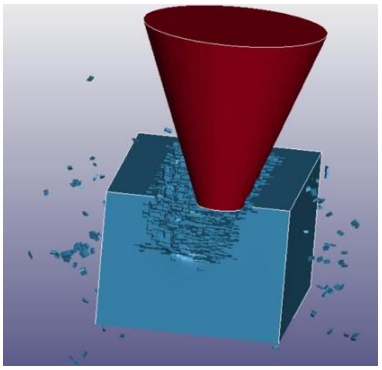


Fig. 13 Removing part of the workpiece material

Alt-text: *3D simulation view of a red conical grain penetrating a blue workpiece, with removed material scattered as small chips around the contact zone.*

Fig. 14 shows the distribution of the von Mises equivalent stresses along the length of the furrow on the workpiece.

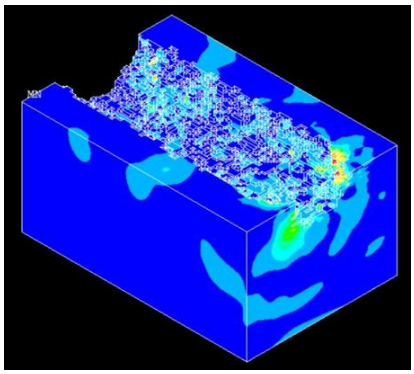


Fig. 14 Distribution of equivalent von Mises stresses along the length of the workpiece groove
Alt-text: *3D colour map of von Mises stress along the workpiece groove; a blue block with a band of higher stress and green-to-red hotspots along the furrow.*

In [7], a study was conducted on chip formation during cutting of aluminum alloy A357, where it was shown that a complete chip shape in this case is formed only if the rake angle of the tool is not less than 70°.

Surface roughness after processing
Of particular interest is the quality of the resulting surface after machining the workpiece in the area of the formed groove. Fig. 15 shows the groove profile in its longitudinal direction in the plastic layer of the material for both grain shapes with a friction coefficient of 0.3 and a depth of 0.001, 0.002, and 0.004 mm at a speed of 5 m/s.

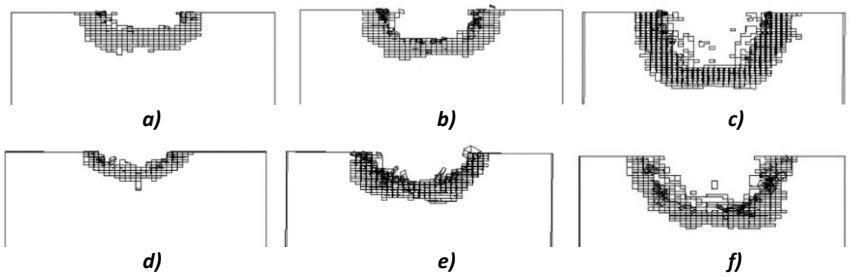


Fig. 15 Surface quality of the treatment at a speed of 5 m/s and a penetration depth of 0.001, 0.002, 0.004 mm for grain: a)-c) - conical; d)-f) – ellipsoidal
Alt-text: *Six cross-sectional groove profiles at 5 m/s: a–c conical grain at depths 0.001, 0.002, 0.004 mm; d-f semi-ellipsoid grain at the same depths.*
Long description: *each panel shows the machined groove as a meshed cross-section. The grooves become wider and deeper as penetration depth increases from 0.001 to 0.004 mm; the conical-grain grooves (a-c) appear more regular than the ellipsoidal-grain grooves (d-f).*

An analysis of the Figures shows that when machining with a conical grain, the surface finish is high at depths of 0.001 and 0.002 mm, and somewhat less so at a depth of 0.004 mm. Considering that the size of the finite element visible protruding above the horizontal surface in the Figure is 2.5 x 10-4 mm in height, this value can be used to judge the finish. It is also clear that for an ellipsoid, the surface finish decreases, and this can be judged by the size of the finite elements protruding above the surface.

CONCLUSION
This article demonstrates that finite element modeling in LS-DYNA enables quantitative evaluation of the force, energy, and thermal characteristics of the polishing process for 6061-T6 aluminum alloy using single grains of varying shapes and links them to the resulting surface quality. A 3D model of the grain-workpiece system was constructed using 6061-T6 workpiece material using the Johnson-Cook model coupled with the Mie-Grüneisen equation of state, ensuring accurate accounting of plasticity, fracture,

and pressure at high strain rates. It is shown that when transitioning from a truncated-conical to a semi-ellipsoidal grain at low polishing speeds, the total contact force decreases, while the total contact energy and temperature in the contact zone increase due to changes in the actual contact area and the contribution of frictional energy.

Numerical experiments revealed ranges of speeds, penetration depths, and friction coefficients at which a conical grain provides superior surface finish under moderate thermal loads, while a worn (ellipsoidal) grain produces greater heat and poorer groove microgeometry. It was found that at typical polishing speeds of approximately 5 m/s, the increase in workpiece temperature due to grain wear remains limited, and grain geometry and cutting depth play a dominant role in determining surface quality. This provides a basis for selecting optimal grinding modes and monitoring the condition of the abrasive belt.

ACKNOWLEDGEMENT

The authors would like to thank Dr. Daniela Sršníková for her help with the translation of this article.

FUNDING STATEMENT

This work was supported by project VEGA, No. 1/0423/23.

REFERENCES

[1] Bratan S.M., Chasovitina A.S. (2023) Modeling the relationships between input factors and output indicators of the internal grinding process taking into account mutual vibrations of the tool and the workpiece. *Metalworking* (Technology, Equipment, Tools). 25(1) pp. 57-70. doi:10.17212/1994-6309-2023-25.1-57-70

[2] Bratan S, Ságová Z, Ságа M, Yakimovich B, Kuric I. (2023) New calculation methodology of the operations number of cold rolling rolls fine grinding. *Appl Sci*. 13(6):3484.

[3] Bratan S.M, Chasovitina A.S. (2022) Modeling the influence of relative tool and workpiece vibrations on material removal during internal grinding. *Sci-Intensive Technol Mech Eng*. (9) pp. 3-9. doi:10.30987/2223-46082022-9-3-9

[4] Pakhalyuk A.V., Stadnik T.V. (2025) Brief analysis of polishing methods for long cylindrical aluminum blanks. *Fundam Appl Probl Eng Technol*. (5) pp. 224-228. doi:10.33979/2073-7408-2025-373-5-224-228

[5] Dănuț J. (2017) SPH simulation of single grain action in grinding. *MATEC Web Conf. 2017*;137:03006. doi:10.1051/matecconf/201713703006

[6] Anderson D, Warkentin A, Bauer R. (2012) Comparison of spherical and truncated cone geometries for single abrasive grain cutting. *J Mater Process Technol*. 212 pp. 1946-1953. doi:10.1016/j.jmatprotec.2012.04.021

[7] Cheng-Ming H. (2021) A357 aluminum alloy cutting performance finite element simulation. *Glob J Eng Sci*. 7(3) pp. 1-13. doi:10.33552/GJES.2021.07.000667

[8] Bachurová N, Kudláček J, Kuchař J, Červený J. (2025) The effect of surface pretreatments on the reliability of glass bonded joints. *Coatings*. 15:232. doi:10.3390/coatings15020232

[9] Kuchař J, Kreibich V, Agartanov V, Petřík M. (2018) Maintenance and cleaning of heat exchangers. *Mater Sci Forum*. 919 pp. 396-401. doi:10.4028/www.scientific.net/MSF.919.396

[10] Kuchař J, Kreibich V, Procházková D, Bachurová N. (2023) Mitigating the risks of energetic facilities by cleaning internal surfaces. In: *Proc Int Conf Saf Reliab*. doi:10.3850/978-981-18-8071-1_P254-cd

[11] Kuchař J, Kreibich V, Procházková D, Tláskal F. (2023) Mitigation of risks of corrosion and delamination by surface pre-treatment. In: *Proc Int Conf Saf Reliab*. doi:10.3850/978-981-18-8071-1_P112-cd

[12] Zhang Z, Zhang W, Zhang S, Li F. (2019) Chemical mechanical polishing of aluminum alloys using alumina-based slurry. *Tribology*. 39(1) pp. 109-117. doi:10.16078/j.tribology.2018032

[13] Wu Z, Shen J, Wu X, Peng Y, Lin S, Huang X, et al. (2023) Research on polishing aluminum alloy optical elements with a new solid flexible bonnet tool. *J Manuf Process*. pp. 168-180. doi:10.1016/j.jmapro.2023.08.037

[14] Beigmoradi S, Vahdati M. (2022) Experimental and numerical study of polishing of 2024 aluminum alloy using acoustics energy. *J Manuf Process*. 73 pp. 440-453. doi:10.1016/j.jmapro.2021.11.009

[15] Yuan Q, Qi H, Wen D. (2016) Numerical and experimental study on the spiral-rotating abrasive flow in polishing of the internal surface of 6061 aluminium alloy cylinder. *Powder Technol*. 302 pp. 153-159. doi:10.1016/j.powtec.2016.08.047

[16] Lin J.W. (2023) Aluminum tube polishing fire problem: a case study. *Eur J Eng Technol Res*. 8(2) pp. 58-59. doi:10.24018/ejeng.2023.8.2.3022
[17] Brusov A, et al. (2021) Electropolishing of single crystal and polycrystalline aluminum to achieve high optical and mechanical surfaces. arXiv [Preprint]. arXiv:2102.05752.
[18] Iquebal A.S, Sagapuram D, Bukkapatnam S. (2019) Surface plastic flow in polishing of rough surfaces. *Sci Rep*. 9:10617. doi:10.1038/s41598-019-46997-w
[19] Song P, Yang C, Bai Y, Ding J, Guo J, Li C, et al. (2023) High-precision turning and ultra-smooth direct polishing of aluminum alloy mirrors. *Opt Express*. 31(19) pp. 30340-30358. doi:10.1364/OE.495779
[20] Burzic B, Hofele M, Mürdter S, Riegel H. (2017) Laser polishing of ground aluminum surfaces with high energy continuous wave laser. *J Laser Appl*. 29(1).
[21] Dev A, Tandon S, Kumar P, Dutt A. (2020) of coating and polishing of cutting tool on machined surface quality in dry machining of aluminium alloy. *Def Sci J*. 70(3) pp. 299-305. doi:10.14429/dsj.70.14831
[22] Abbas A.M, Khleif A.A. (2024) Multi-optimization method for new design of angled electrodes and performance enhancement using alloy steel (X210). *Management Systems in Production Engineering*. Volume 32, Issue 3. pp. 438-449. doi: 10.2478/mspe-2024-0041
[23] Yu N, Li L, Kee CS. (2021) Modeling and simulation of the surface generation mechanism of a novel low-pressure lapping technology. *Micromachines*. 12:1510. doi:10.3390/mi12121510
[24] Abdullah M.A, Abed A.H, Mansor K.K. (2025) Comparison between low-carbon steel end galvanized steel by deep drawing under the influence of different parameters. *Management Systems in Production Engineering* Volume 33, Issue 2, pp. 163-170 DOI 10.2478/mspe-2025-0016
[25] Enzi A, Abdulameer A.G, Hassoon O.H, Hamieh A. (2025) Experimental investigation of manufacturing variables effect on electrical discharge machining of titanium alloy. *Management Systems in Production Engineering* Volume 33, Issue 2, pp. 202-211 DOI 10.2478/mspe-2025-0019
[26] González Rojas H.A, Sánchez Egea A.J, Travieso-Rodríguez J.A, Llumà i Fuentes J, Jorba Peiró J. (2018) Estimation of the polishing time for different metallic alloys in surface texture removal. *Mach Sci Technol*. 22(4) pp. 729-741. doi:10.1080/10910344.2017.1402931
[27] Zhu Y.F, Sheng P.F, Huang Q.S, Wang L, Yu J, Zhang Z, et al. (2025) Theoretical and experimental study of the evolution of surface textures during wheel polishing with fluid cutting model. *Adv Manuf*. pp. 1-17. doi:10.1007/s40436-025-00574-9
[28] Bal B, Karaveli K.K, Cetin B, Gumus B. (2019) The precise determination of the Johnson-Cook material and damage model parameters and mechanical properties of aluminum 7068-T651 alloy. *J Eng Mater Technol*. 141(4). doi:10.1115/1.4042870
[29] Lesuer D.R, Kay G.J, LeBlanc M.M. (1999) Modeling large-strain, high-rate deformation in metals. In: Proc 3rd Biennial Tri-Laboratory Eng Conf Modeling Simulation. Pleasanton (CA): Lawrence Livermore National Laboratory; pp. 3-5.
[30] Fraser K, St-Georges L, Kiss L.I. (2015) Numerical simulation of bobbin tool friction stir welding [Internet]. [cited 2025 Nov 16]. Available from: https://www.researchgate.net/publication/275271390
[31] Altair Engineering. EOS/Gruneisen block format keyword [Internet]. (2023) [cited 2025 Nov 16]. Available from: https://2023.help.altair.com/2023/hwsolvers/rad/topics/solvers/rad/eos_gruneisen_starter_r.htm
[32] Rubin M.B, Herbolt E.B. (2020) An analytical expression for temperature in a thermodynamically consistent model with a Mie-Gruneisen equation for pressure. *Int J Impact Eng*. 143:103612. doi:10.1016/j.ijimpeng.2020.103612
[33] Anand R.K, (2025) On the jump conditions for shock waves in condensed materials [Internet]. [cited 2025 Nov 16]. Available from: https://arxiv.org/html/2502.09677v1
[34] Kopas P, Blatnicky M, Sága M, Vasko M. (2017) Identification of mechanical properties of weld joints of AlMgSi07.F25 aluminium alloy. Metalurgija. 56(1-2) pp. 99-102.
[35] Sága M, Kopas P, Uhrícík M. Modeling and Experimental Analysis of the Aluminium Alloy Fatigue Damage in the case of Bending – Torsion Loading. *Modelling of Mechanical and Mechatronics Systems*, Vol. 48, pp. 599-606, DOI10.1016/j.proeng.2012.09.559

Sergei Bratan
Sevastopol State University
33 Universitets'ka St 299053
Sevastopol, Crimea

Milan Sága
University of Žilina
Faculty of Mechanical Engineering
Univerzitná 8215/1, 010 26 Žilina, Slovakia

Andrei Pakhaliuk
Sevastopol State University
33 Universitets'ka St 299053
Sevastopol, Crimea

Vladimir Pakhaliuk
Sevastopol State University
33 Universitets'ka St 299053
Sevastopol, Crimea

Jiří Kuchař (corresponding author)
Czech Technical University in Prague
Faculty of Mechanical Engineering
Prague, Czech Republic
e-mail: Jiri.Kuchar@fs.cvut.cz

Boris Yakhimovich
Sevastopol State University
33 Universitets'ka St 299053
Sevastopol, Crimea